ARTICLE   OPEN

Check for updates

Topological electronic structure of $YbMg_2Bi_2$ and $CaMg_2Bi_2$

Asish K. Kundu [1] ✉, Tufan Roy [2], Santanu Pakhira [3], Ze-Bin Wu [1], Masahito Tsujikawa[2,4], Masafumi Shirai[2,4,5], D. C. Johnston[3,6], Abhay N. Pasupathy [1,7] and Tonica Valla [1]

Zintl compounds have been extensively studied for their outstanding thermoelectric properties, but their electronic structure remains largely unexplored. Here, we present a detailed investigation of the electronic structure of the isostructural thermopower materials $YbMg_2Bi_2$ and $CaMg_2Bi_2$ using angle-resolved photoemission spectroscopy (ARPES) and density functional theory (DFT). The ARPES results show a significantly smaller Fermi surface and Fermi velocity in $CaMg_2Bi_2$ than in $YbMg_2Bi_2$. Our ARPES results also reveal that in the case of $YbMg_2Bi_2$, Yb-4f states reside well below the Fermi level and likely have a negligible impact on transport properties. To properly model the position of 4f-states, as well as the overall electronic structure, a Hubbard U at the Yb sites and spin-orbit coupling (SOC) have to be included in the DFT calculations. The theoretical results reveal that both materials belong to a Z_2 topological class and host topological surface states around E_F. Due to the intrinsic hole doping, the topological states reside above the Fermi level, inaccessible by ARPES. Our results also suggest that in addition to SOC, vacancies and the resulting hole doping play an important role in the transport properties of these materials.

INTRODUCTION

Intermetallic Zintl-phase compounds have been extensively studied because of their superior thermoelectric (TE) and magnetic properties and their possible use in various applications such as power generation, waste-heat conversion, and solid-state Peltier coolers[1–5]. Recently, the research in this field has been stimulated by the discovery of nontrivial topological phases in various thermopower materials such as $EuIn_2As_2$[6,7], $EuSn_2As_2$[8,9], and other $CaAl_2Si_2$-type compounds[10–14]. The possibility of a strain-induced topological phase transition is also predicted for AMg_2Bi_2 (A = Ca, Sr, Ba) compounds[15]. Materials with nontrivial band topologies exhibit highly desirable properties, such as high carrier mobility, giant linear magnetoresistance, anomalous Hall effects, robust surface states, and high thermopower[16–18].

Among Zintl families, AB_2X_2 (A = Ca, Yb, Eu, Sr; B = Zn, Mn, Cd, Mg; X = Sb, Bi) type compounds gain more attention as many of them show high thermoelectric performance[19–27]. Recent works have demonstrated the coexistence of intrinsic magnetism, topological Dirac electronic states, and moderate thermopower efficiency in $EuMg_2Bi_2$[5,12,13,21,28], which could provide an interesting playground to investigate the interplay between magnetism, topology, and thermoelectricity. Interestingly, it has been found that when the A-sites of these compounds contain rare-earth elements or are partially substituted by rare-earth elements, they show enhanced carrier mobility and carrier concentration compared to the alkaline-earth compounds[26,29,30]. For example, going from $CaMg_2Bi_2$ to $YbMg_2Bi_2$, both the mobility and hole concentration are increased by a factor of ~2[30]. This is quite unexpected, as for chemically-doped semiconductors, the mobility generally decreases with increasing carrier concentration[31].

The stronger hybridization between Bi and Yb/Eu was considered to be partially responsible for higher mobilities in Yb/Eu-based compounds[21]. On the other hand, if the 4f states were near the valence-band maximum, one could expect lower

mobilities due to heavy bands and stronger scattering (impurity, electron-phonon, electron-magnon), exactly opposite to the experimental results[21,30]. Flage et al.[32] have reported that in the prototype system $YbZn_2Sb_2$, the Yb-4f states make a non-negligible contribution to the valence band edge. The exact effects of heavy 4f electrons on carrier concentrations and transport properties in rare-earth-based compounds are still unclear due to the lack of experimental studies.

To achieve a better TE performance, high carrier mobility, heavy effective mass, and low lattice thermal conductivity are highly desirable[1,21]. Various strategies have been proposed to achieve this goal, such as band convergence and resonant states for heavy effective mass[33–35], band alignment to achieve high carrier mobility[21,36] and introducing microstructural defects (point defects and nanostructures) and alloying to enhance phonon scattering[21,34,37]. However, many of the theoretical calculations[25,38–40] do not take into account the effects of spin-orbit coupling (SOC) in the prediction of the transport properties. The effect of SOC could change the band degeneracy (which is related to carrier concentration), band hybridization, and band gap. Thus, the consideration of the effects of SOC is necessary for accurate predictions of new relevant materials and their associated properties. In addition to the more realistic modeling, the experimental measurement of the electronic structure is an irreplaceable component of studies of new materials.

Here, we report comprehensive experimental and theoretical studies of the electronic structures of $YbMg_2Bi_2$ and $CaMg_2Bi_2$ using ARPES and first-principles calculations. Our results show the importance of inclusion of the SOC in describing these materials. We also show that the Yb-4f states are far away from E_F, implying that they do not play a role in transport. Our studies show that both materials are narrow band-gap topological insulators with topological surface states.

[1]Condensed Matter Physics and Materials Science Division, Brookhaven National Laboratory, Upton, NY 11973, USA. [2]Research Institute of Electrical Communication, Tohoku University, Sendai 980-8577, Japan. [3]Ames Laboratory, Iowa State University, Ames, IA 50011, USA. [4]Center for Spintronics Research Network, Tohoku University, Sendai 980-8577, Japan. [5]Center for Science and Innovation in Spintronics, Core Research Cluster, Tohoku University, Sendai 980-8577, Japan. [6]Department of Physics and Astronomy, Iowa State University, Ames, IA 50011, USA. [7]Department of Physics, Columbia University, New York, NY 10027, USA. ✉email: akundu@bnl.gov
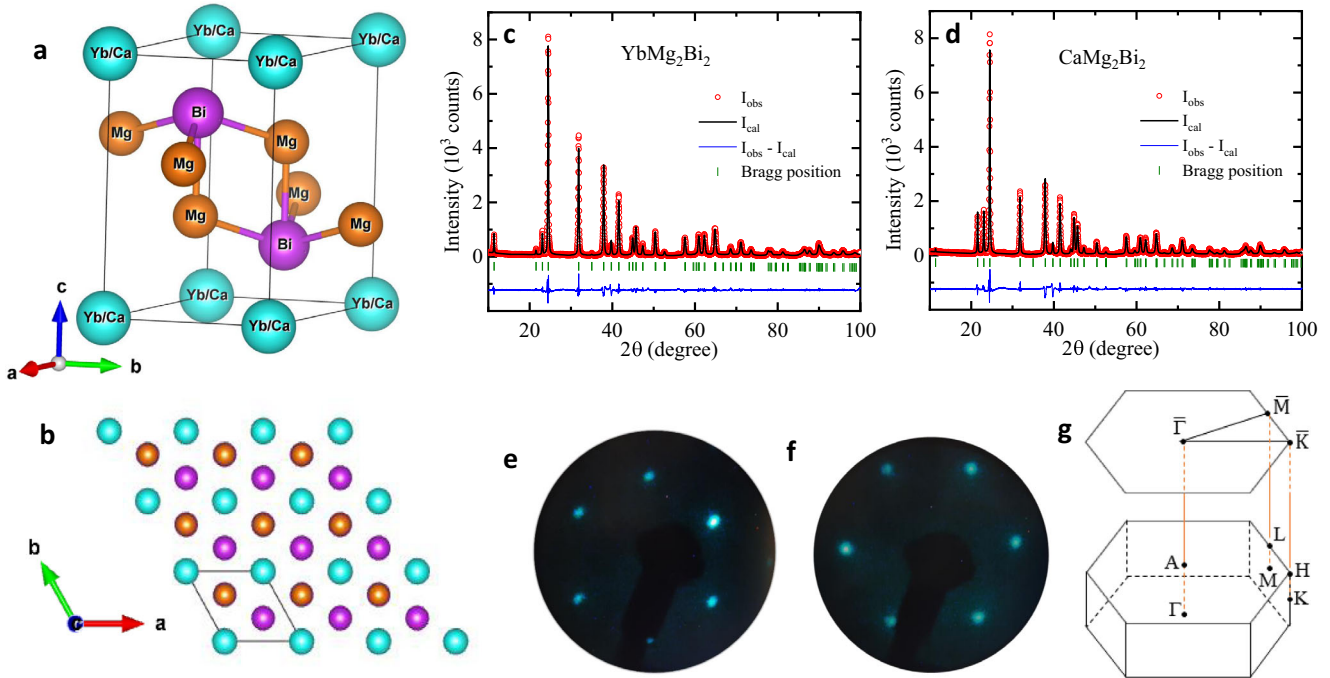
Fig. 1 Crystal structure of AMg$_2$Bi$_2$ (A = Yb, Ca). a Unit cell of trigonal AMg$_2$Bi$_2$. **b** Projection of the crystal structure onto the a-b plane with a unit cell indicated by a rhombus. The crystal structures were generated using the VESTA software[41]. **c, d** XRD patterns of powdered YbMg$_2$Bi$_2$ and CaMg$_2$Bi$_2$ crystals, along with the refinement of the data using FULLPROF software[42]. **e, f** Hexagonal LEED patterns of YbMg$_2$Bi$_2$ and CaMg$_2$Bi$_2$ single crystals obtained after cleaving the samples in-situ under UHV, respectively. **g** Schematics of hexagonal bulk Brillouin zone and its surface projection (SBZ).

RESULTS AND DISCUSSIONS

Structural details of samples

Figure 1 shows the schematics of the crystal structure, x-ray diffraction (XRD) and the low-energy electron diffraction (LEED) patterns of the AMg$_2$Bi$_2$ (A = Yb, Ca) samples. Figure 1a, b show the trigonal unit cell and the top views of the (001) surface (a-b plane) of the crystal structure, respectively[41]. Using the Zintl concept, the trigonal structure of AMg$_2$Bi$_2$ compounds can be viewed as polyanionic [Mg$_2$Bi$_2$]$^{2-}$ layers stacked along the c-axis and separated by the trigonal layers of A^{2+}. The room-temperature powder XRD patterns taken on crushed YbMg$_2$Bi$_2$ and CaMg$_2$Bi$_2$ single crystals are shown in Fig. 1c, d, respectively. The experimental data fit well with the CaAl$_2$Si$_2$-type crystal structure having a trigonal lattice with space group $P\bar{3}m1$ (No. 164)[42]. The refined lattice parameters are $a = b = 4.7258(4)$ Å and $c = 7.6453(14)$ Å for YbMg$_2$Bi$_2$ and $a = b = 4.7236(3)$ Å and $c = 7.6512(10)$ Å for CaMg$_2$Bi$_2$, in good agreement with the earlier-reported values[30]. LEED patterns taken from in-situ UHV-cleaved YbMg$_2$Bi$_2$ and CaMg$_2$Bi$_2$ crystals are shown in Fig. 1e, f, respectively. Hexagonal patterns are obtained for both samples, confirming that the cleaved surface is the (001) plane. The schematics of the hexagonal bulk Brillouin zone and its surface projection, i.e. surface Brillouin zone (SBZ), are shown in Fig. 1g.

Theoretical bulk electronic structures

Figure 2 shows the bulk electronic structure along various symmetry paths for AMg$_2$Bi$_2$. Figure 2a, b illustrate the band dispersions of YbMg$_2$Bi$_2$, without and with spin-orbit coupling (SOC), respectively. A Hubbard U parameter of 4 eV is included to describe the localized $4f$ states of Yb and to match the observed splitting. Multiple Dirac-like band crossings are observed (e.g., at K and between K and M symmetry points) in the absence of SOC; however, most of the Dirac points become gapped in the presence of SOC due to lifting of band degeneracy. The Yb-$4f$ derived flat band that was initially at about -1.3 eV (Fig. 2a) splits

into two levels, $4f_{5/2}$ (-2.85 eV) and $4f_{7/2}$ levels (-1.25 eV) in the presence of SOC. We also see the strong hybridization between the $4f$ states and highly-dispersive bands when they cross each other. To better understand the role of $4f$ states, we have also treated the $4f$ electrons as core electrons and the resulting band structure is shown in Fig. 2c. Note that the low-energy electronic structure is very similar to the one in which the $4f$ electrons are considered as valence electrons (Fig. 2b), except for a slight downward shift of the hole-bands around the Γ point. To understand whether this apparent energy shift is related to the intrinsic properties of the $4f$ electrons, we performed the calculation considering higher U values (see Supplementary note 1). By increasing the U value from 4 eV to 8 eV, we essentially move the $4f$ states much deeper in energy, but still observe a similar low-energy electronic structure without any energy shift of the hole-bands. This suggests that the energy shift is related to inclusion of the external parameter U in the DFT calculation. Without SOC a spectral gap of about 0.1 eV can be observed between the valence and conduction bands, and the system behaves like a semiconductor while it is nearly gapless in the presence of SOC. Interestingly, a closer look around the Γ point (inset of Fig. 2c) reveals that a small energy gap of about ~15 meV is still present and the shapes of the valence band maximum (VBM) and conduction band minimum (CBM) suggest that there might be a band inversion. The parity of the bands at Γ also reverses when SOC is turned on, suggesting a band inversion scenario. Similar electronic structures have also been demonstrated in previous theoretical studies; however, they were conducted without SOC[21].

Similarly, Fig. 2d, e illustrate the electronic structure of CaMg$_2$Bi$_2$ without and with SOC, respectively. A spectral gap of about 0.5 eV can be seen between the VBM and CBM in the absence of SOC while the gap is extremely reduced when SOC is turned on. This is consistent with the previous reports[21,27]. The only major difference between these two systems is the absence of flat $4f$
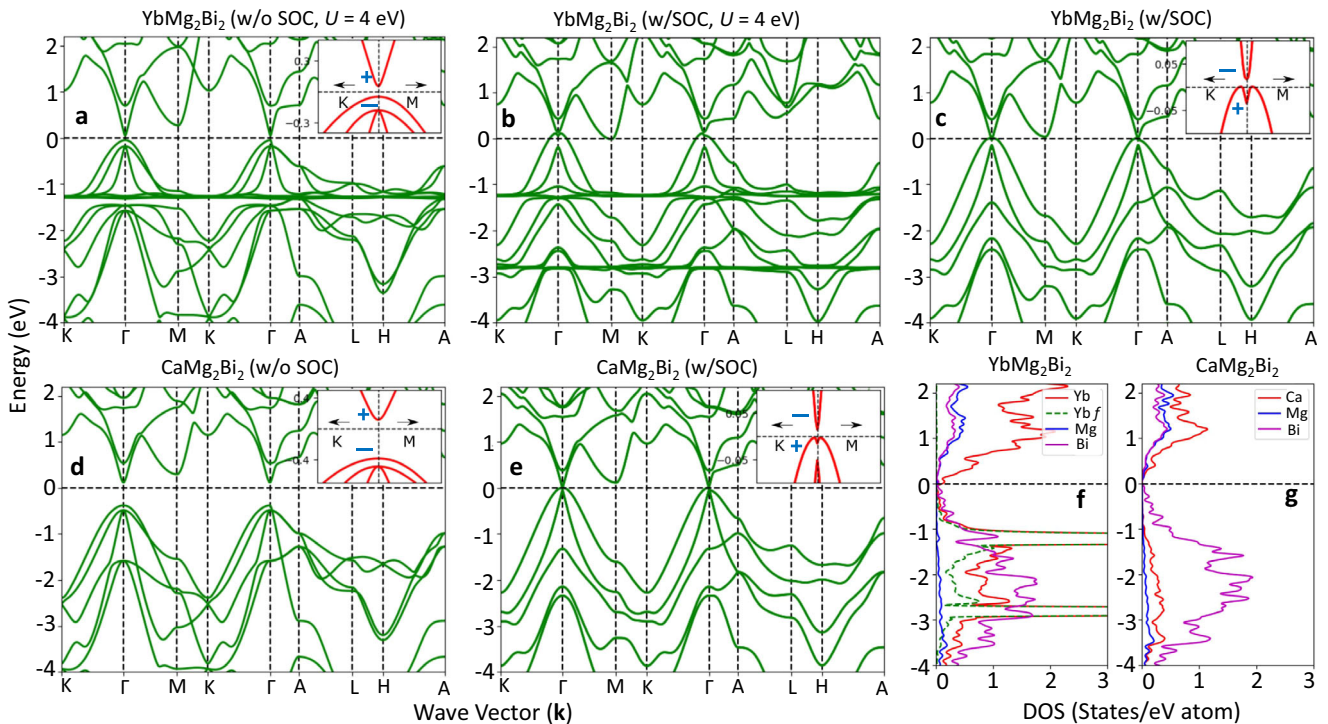
Fig. 2 Bulk band-structure calculations of AMg_2Bi_2 crystals. a, b Band dispersions of $YbMg_2Bi_2$, without and with SOC, respectively. A Hubbard $U = 4$ eV is included to treat the strongly-correlated Yb-4f states. **c** Same as **b**, but taking 4f electrons as core electrons. **d, e** Band dispersions of $CaMg_2Bi_2$ without and with SOC, respectively. The insets of **a, c, d, e** show the zoomed-in view of the fundamental band-gaps for the corresponding models. The parities of the topmost valence band and the first conduction band at the Γ point are marked. **f, g** Partial density of states (PDOS) plots of $YbMg_2Bi_2$ (including f-electrons) and $CaMg_2Bi_2$, respectively.

bands in the case of $CaMg_2Bi_2$. The band inversion is also reduced but is still present as shown in the inset of Fig. 2e.

To correctly verify the nontrivial topology of these materials hinted by the shape of the valence/conduction bands near the zone center, we have calculated the Z_2 topological numbers using the Wilson loop (Wannier charge center) method[43] for the six time-reversal invariant momentum planes. The obtained results show Z_2 topological numbers $\nu_0;(\nu_1\nu_2\nu_3) = 1;(000)$ for both systems, which indicates that both materials are strong topological insulators. Here, we want to point out that although the low-energy electronic structure is very similar to the type-II nodal-line semimetal Mg_3Bi_2[11], the present materials are not nodal-line semimetals due to the presence of a band gap ~0.10–0.5 eV without SOC. In contrast, nodal-line semimetals should show conduction and valence-band crossing in the absence of SOC.

Figure 2f, g show the partial densities of states (PDOS) of $YbMg_2Bi_2$ and $CaMg_2Bi_2$, respectively, in the presence of SOC. Both systems show very similar PDOS for Bi and Mg atoms, while they differ significantly for Ca and Yb atoms. Yb contributes more to the valence and conduction bands than Ca. The contribution of Yb-f states is strongly localized around −1 eV, and it diminishes around the band edges. This implies a negligible role of 4f electrons in the transport properties in this material. In order to obtain a better understanding of the orbital character of the bands and their hybridization, orbital-resolved band dispersions are shown with and without SOC for $YbMg_2Bi_2$ (Fig. 3a–f) and $CaMg_2Bi_2$ (Fig. 3g–l) systems, respectively. The contributions from Ca/Yb-s, Bi-p, and Mg-s are shown. It can be seen that the outer hole-like valence band has dominant Bi-p character while the inner one has mixed Bi-p, Mg-s, and Ca-s/Yb-s character. It appears that all orbitals are strongly hybridized with each other, both in the presence and absence of SOC. We note that some contributions of other orbitals such as Bi-s, Mg-p, Ca-p, Yb-d, and Yb-p are also present around E_F (not shown).

Comparison between the experimental and theoretical band dispersions: $YbMg_2Bi_2$

Figure 4 shows the comparison between the experimental and the calculated electronic structure of $YbMg_2Bi_2$. Panel 4 **a** represents the measured ARPES spectrum along the $\bar{\Gamma} - \bar{M}$ line, which, at the photon energy used in the experiments, is very close to the bulk Γ-M line. The calculated bulk electronic structure along the Γ-M line is superimposed for comparison. To match the experimental dispersions, the theoretical spectrum is shifted up by ~0.3 eV, implying that the measured sample is heavily hole-doped. According to the previous reports, intrinsic hole doping in these samples is predominantly due to A-site vacancies[21,30]. In addition to numerous dispersing bands, two flat bands at energies −1.15 eV and −2.5 eV are visible in the ARPES spectrum. These flat bands are better resolved when probed with the He-II photon energy (40.8 eV) as shown in Supplementary note 2. They arise from spin-orbit-split Yb-4f states, matching nicely with the calculations when SOC and $U = 4$ eV are taken into account. It is also visible that the dispersive bands and the Yb-4f bands hybridize, in accord with our theoretical results. We note that the position of the Yb-4f states varies among different Yb-compounds[26,44], implying that U is not unique. In previous studies, a reasonable value of U has been found to be 5.3 eV for $YbZn_2Sb_2$[26] and 8 eV for YbB_{12}[44]. High-resolution ARPES spectra in the vicinity of E_F, near the zone center in the first and second SBZ, are shown in panels **b** and **c**, respectively. Both spectra show linearly-dispersive hole-like bands crossing the Fermi level without any measurable renormalization, indicative of weak electron correlation in $YbMg_2Bi_2$. A visible change in the Fermi wave vector (k_F) of both the inner and outer bands between the first and second SBZ originates from the difference in probed k_Z for the two spectra and points to their bulk electronic origin. This change of k_Z can be better realized from the momentum-dispersion curves (MDC) around E_F as shown in Supplementary note 3. The
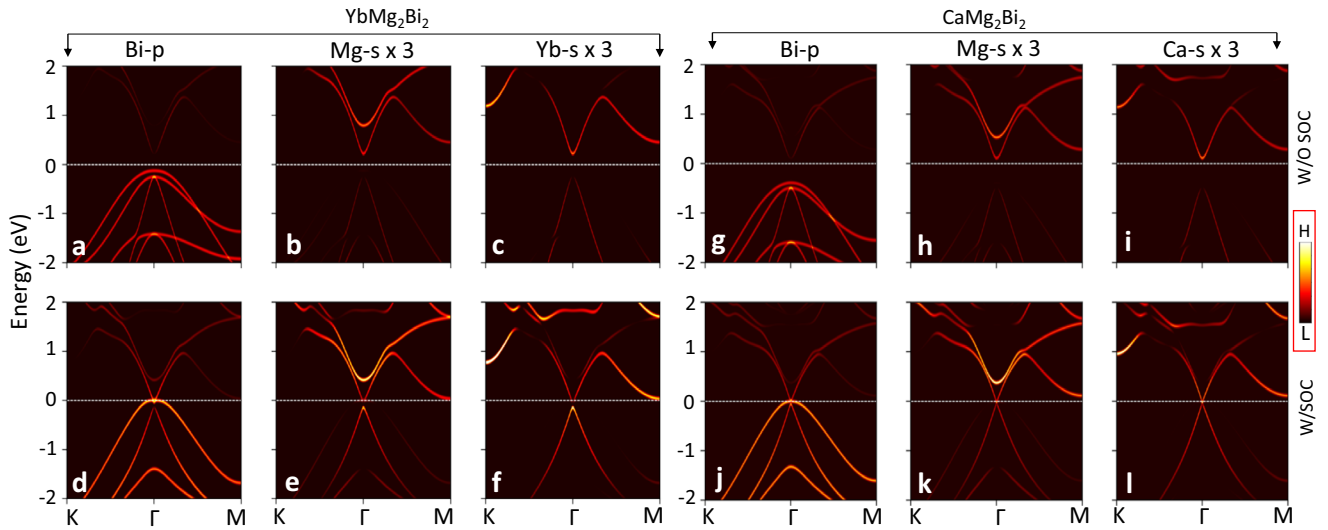
Fig. 3 Orbital-resolved band-structure of AMg_2Bi_2. a–c and **d–f** Band dispersions of Bi-p, Mg-s and Yb-s orbitals without and with SOC for $YbMg_2Bi_2$, respectively. **g–i** and **j–l** Band dispersions of Bi-p, Mg-s and Ca-s orbitals without and with SOC for $CaMg_2Bi_2$, respectively. The spectral intensity of the Mg-s and Yb-s bands is multiplied by a factor of three to enhance the visibility.
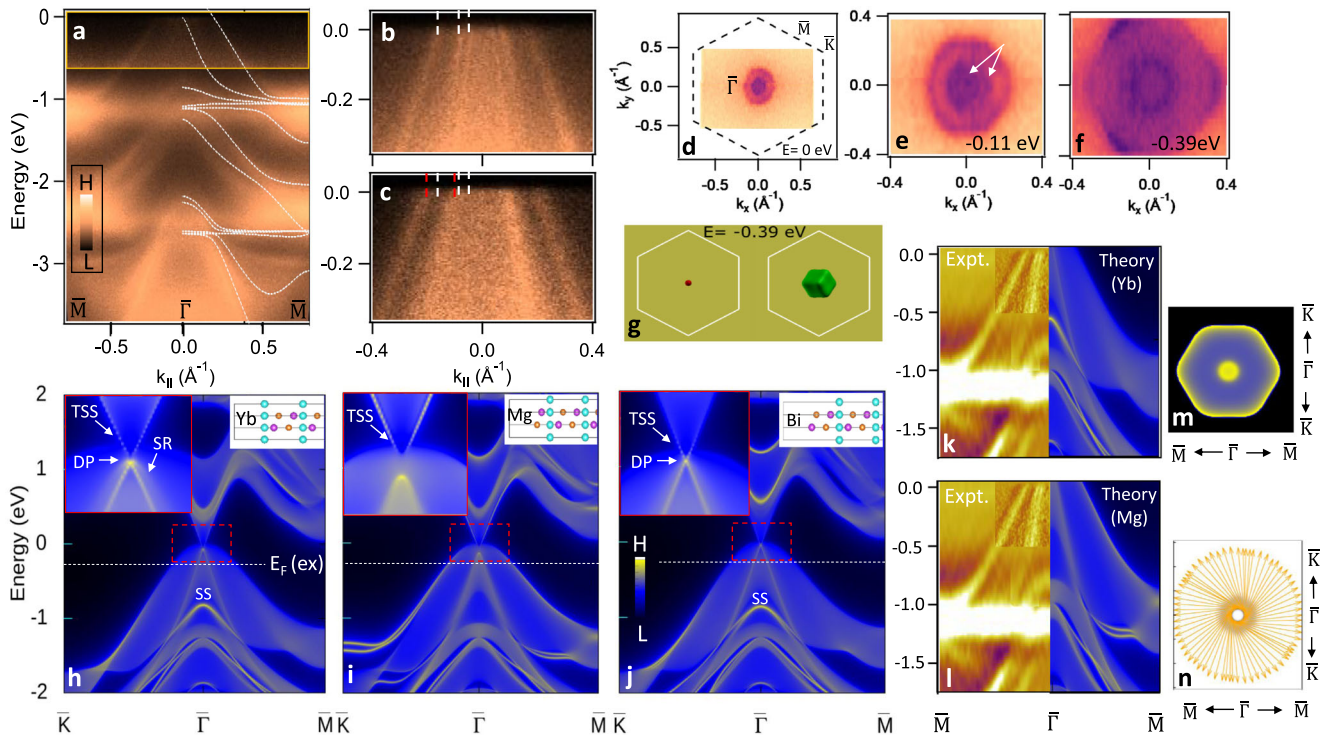

Fig. 4 Comparison of experimental and calculated electronic structure for $YbMg_2Bi_2$. a ARPES spectrum (from first SBZ) along the $\overline{M} - \overline{\Gamma} - \overline{M}$ line. The contrast at low binding energies is enhanced to improve visibility. Theoretical bulk bands (white dotted lines) along the Γ-M path are superimposed on top. **b, c** ARPES spectra close to E_F around $\overline{\Gamma}$ from the first and second SBZ, respectively. The white and red vertical dashed lines indicate the k_F positions inside the first and second SBZ, respectively. **d** Fermi surface measured by ARPES (intensity integrated within ± 10 meV around E_F). The SBZ is indicated by the dashed hexagon. **e, f** Constant-energy contours at $E = -0.11$ and -0.39 eV, respectively. Arrows in **e** indicate two nearly circular contours. Light and dark colors in **d–f** indicate low and high photoemission intensity, respectively. **g** Calculated 3D constant-energy contour at $E = -0.39$ eV viewed perpendicular to the (001) surface. Spherical (left) and hexagonal (right) shaped contours are formed by the inner and outer hole-like bands at Γ. **h–j** Calculated surface state spectrum from a (001) semi-infinite slab of Yb-, Mg-, and Bi-terminated surfaces, respectively. Insets show the structure of different terminations (right) and zoomed-in spectra around $\overline{\Gamma}$ (left), within the dashed rectangles. The topological surface-state (TSS) is visible within the bulk gap. A surface-resonance band (SR) is marked in the inset of **h**. The Dirac point (DP) is marked in the inset of **h, j**. The horizontal dashed lines represent the positions of the experimental Fermi level. **k, l** Side-by-side comparison of the measured ARPES spectra with the calculated surface state spectra for Yb and Mg terminations, respectively. **m** Calculated constant-energy contours (at $E = -0.3$ eV) for the Mg-terminated surface. Light and dark colors in **k–m** indicate high and low intensity, respectively. **n** Spin texture of TSS for the Mg-terminated surface.

bulk origin of these states is in good agreement with the recent photon-energy-dependent ARPES studies on similar materials[10,11]. These linearly-dispersing bands form nearly-circular Fermi surfaces, Fig. 4d. The constant-energy contours at −0.11 eV and −0.39 eV are also shown in Fig. 4e, f, respectively. The inner two contours are very closely spaced and can only be resolved away from the Fermi level. The outer contour exhibits hexagonal warping that strengthens with increasing binding energy. The 3-fold symmetry of the intensity of the outer contour also suggests its significant bulk-band character. Similar contours are obtained from the bulk electronic structure near the Γ point of the 3D BZ, as shown in Fig. 4g.

Since ARPES is a surface-sensitive probe and the bulk band-structure calculations imply the existence of topological surface states, we have also calculated the surface electronic structure for various possible terminations of the (001) surface. The Yb-4f states are not included in these calculations for simplicity. Figure 4h–j show the calculated surface electronic spectra from a (001) semi-infinite slab terminated by Yb, Mg, and Bi, respectively, where the enlarged views near the Fermi energy around $\bar{\Gamma}$ are shown in the left insets of each figure. The spectral brightness indicates the integrated charge density over the top six atomic layers, roughly equivalent to the ARPES probing depth.

It is clear that a topological surface state (TSS), spanning the bulk band gap, is present on every termination. The Dirac point is buried inside the valence band, but should be exposed on Yb-and Bi-terminations. A similar TSS was also reported in other topological materials where the Dirac point lies inside the valence band, such as p-type Bi_2Te_3 and Mg_3Bi_2[11,18,45]. The topological character of TSS is further supported by its helical spin-texture as shown in Fig. 4n. Overall, the calculated spectra for different terminations are very similar, resembling the bulk band features. A few noticeable differences are: (1) in the case of Mg termination, the outer state seems sharper, while for Yb and Bi terminations the inner state is more pronounced and (2) the Yb and Bi terminations

show an intense surface state around $\bar{\Gamma}$ at −0.85 eV, while the Mg termination does not. A direct side-by-side comparison of the ARPES spectra with the calculated surface state spectra (Fig. 4k, l) indicate somewhat better agreement with the Mg termination. However, the theoretical spectra for the Mg termination show only two states forming the Fermi surface (Fig. 4m), whereas three states are observed experimentally. On the other hand, the Yb terminations display an additional surface-resonance band (SR) (inset of Fig. 4h).

The coexistence of different terminations would probably give the best agreement with the observed spectra, as their contributions would be averaged over the macroscopic size of the excitation spot. To get further insight about the surface structure, we performed atomic force microscopy (AFM) measurements and the results are shown in Supplementary note 6. On the optically-flat surface regions, we observe different step heights, suggesting different surface terminations. The coexistence of different surface terminations has been observed for various materials such as Pt_3Te_4, $YBa_2Cu_4O_8$ and Bi_4Se_3 using micro/nano ARPES and scanning-tunneling microscopy (STM)[46–48]. Similar microscopic studies would be needed to disentangle the contributions from different terminations in the present materials.

Potassium-deposited YbMg$_2$Bi$_2$

Due to high hole doping of pristine samples, the VBM, TSS and conduction band are unoccupied and cannot be probed in conventional ARPES. Therefore, we have performed in-situ electron-doping of cleaved surfaces by potassium deposition. The obtained results are shown in Fig. 5. Figure 5a shows the spectrum of the pristine YbMg$_2$Bi$_2$ surface in the second SBZ. The second SBZ is chosen because bands near E_F show a higher photoemission intensity. Figure 5b–d show the spectra after 3, 7, and 12 min of potassium deposition, respectively. It can be seen that the states shift towards higher binding energy and become blurred due to the increase in scattering rates. In the
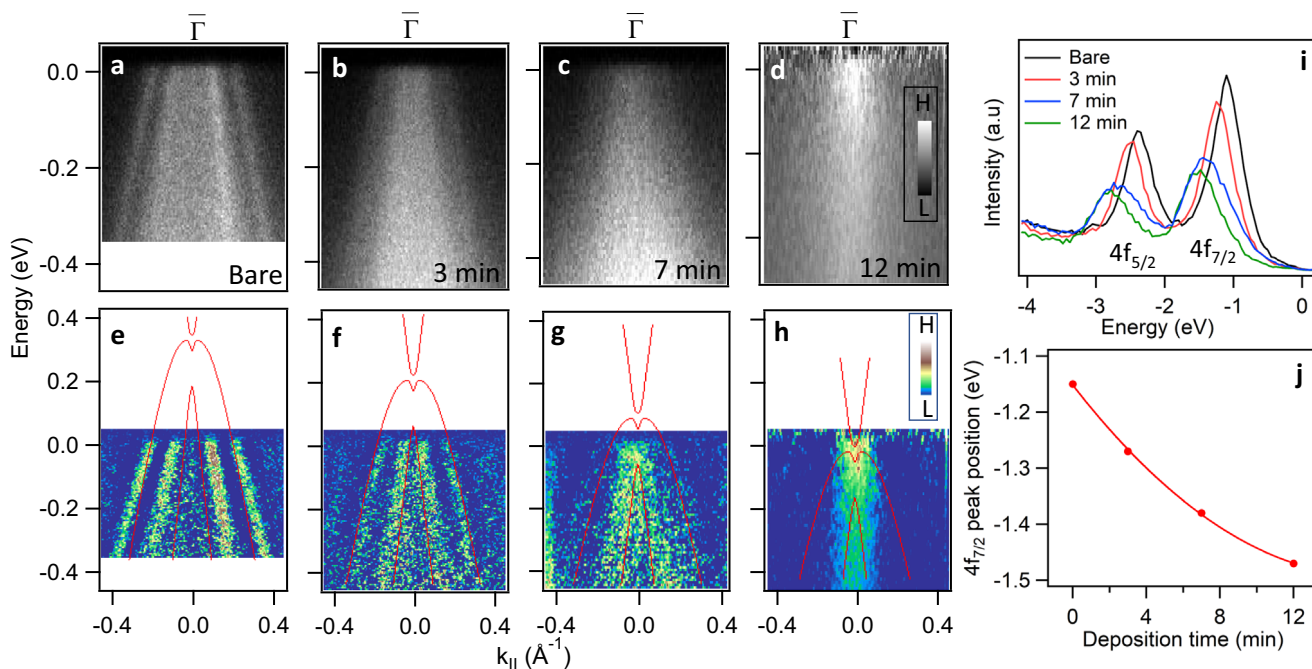

Fig. 5 Potassium deposition on YbMg$_2$Bi$_2$. a–d ARPES spectra for pristine YbMg$_2$Bi$_2$ and after 3, 7, and 12 min of potassium deposition, respectively. In **d**, the ARPES intensity was divided by the Fermi-Dirac distribution function. **e–h** Second derivatives d^2I/dk^2 of the corresponding ARPES spectra along the momentum direction. **i** Corresponding energy distribution curves. **j** Energy of the $4f_{7/2}$ peak obtained from **i**. Theoretical bulk bands (red curves) are overlaid on **e–h** after shifting the energy by amounts from **i**.
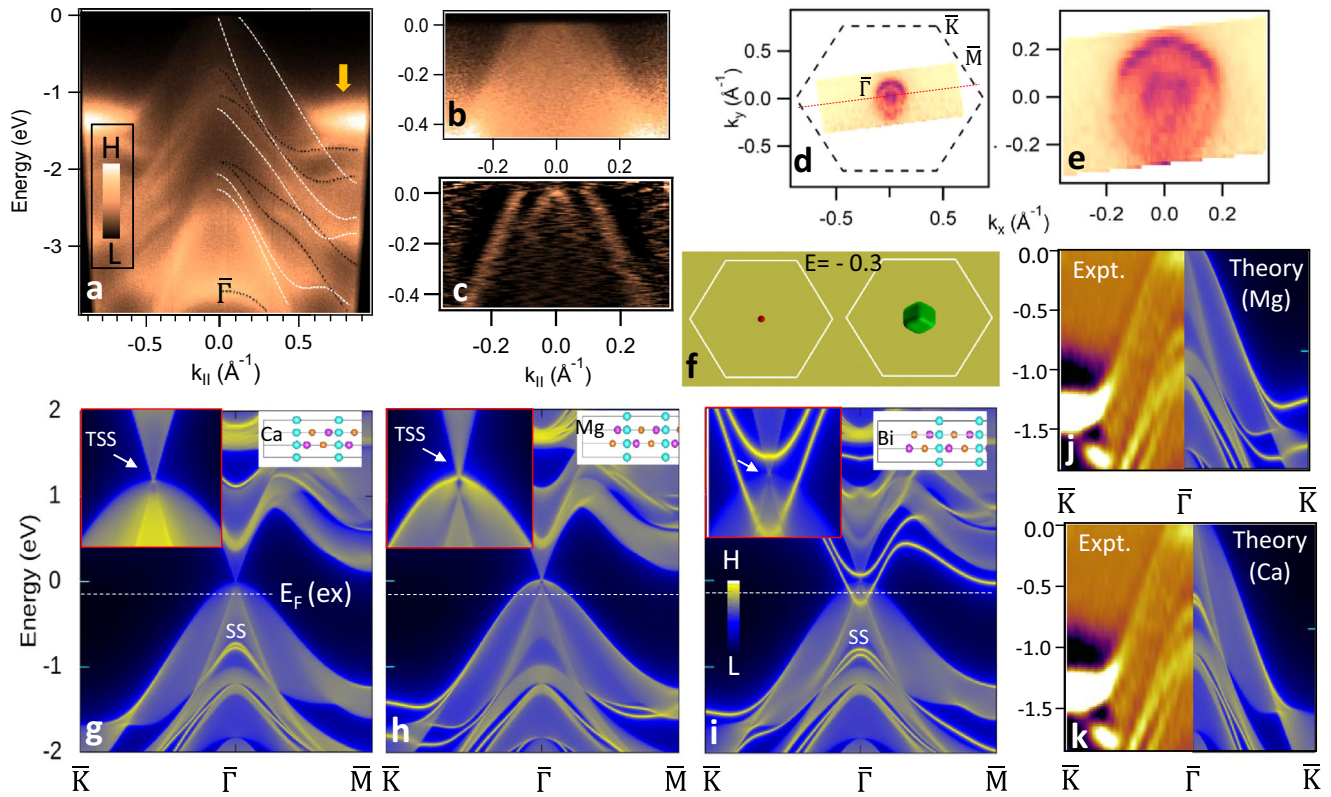
Fig. 6 Comparison of experimental and calculated electronic structure for CaMg₂Bi₂. a ARPES spectrum along a line as shown by the red dashed line in **d**. Theoretical bulk bands along Γ-K (white dotted-lines) and A-H (black dotted-lines) are superimposed after shifting them up by ~ 0.15 eV. Theoretical bulk-bands capture most of the spectral features except for the state indicated by an arrow. **b**, **c** Low-energy ARPES spectrum and its second derivative $[d^2I/dk^2]$, respectively. **d**, **e** Experimental Fermi surface and a constant energy contour at $E = -0.10$ eV, respectively. Light and dark colors in **d**, **e** indicate low and high photoemission intensity, respectively. **f** Calculated bulk constant energy contours at $E = -0.30$ eV. Spherical (left) and hexagonal (right) surfaces are formed by the inner and outer hole-like bands at Γ. **g–i** Calculated surface-state spectra for Ca-, Mg-, and Bi-terminations, respectively. Insets show different terminations (right) and zoomed-in spectra around Γ̄ (left). The dotted lines represent the position of the experimental Fermi level. **j**, **k** Comparison of the ARPES spectra to the calculated surface-state spectra for Ca and Mg terminations, respectively. Light and dark colors in **j**, **k** indicate high and low intensity, respectively.

last sequence, an intensity (V-shaped-like feature) very close to E_F can be seen in Fig. 5d, suggesting that the CBM just becomes occupied. We note that in Fig. 5d, the ARPES intensity was divided by the Fermi-Dirac function to better resolve the spectral feature around E_F. The raw ARPES data shown in Supplementary Fig. 4, are consistent with that conclusion. To better understand the change of electronic structure due to the potassium deposition, we have plotted the second derivatives of the spectra in Fig. 5e–h and the corresponding energy distribution curves (EDCs) in Fig. 5i. The energy shift of the $4f_{7/2}$ peak with potassium deposition time is shown in Fig. 5j. A very similar energy shift is also observed for the Bi 5d core-levels (Supplementary note 5), suggesting a nearly rigid-band-shift scenario. Thus, on top of the second derivative plots (Fig. 5e–h), the calculated bulk bands (red curves) are super-imposed and shifted to match the experimental spectra by using the energies from Fig. 5i. Even though there is a relatively good agreement between theory and experiment, we could not resolve the TSS and conduction band edge individually as the electronic states become too diffuse.

We note that the deposition of potassium on the surface alters the surface potential, causing band-bending in the relatively thick range from the surface (~10–50 nm)[49]. Previous ARPES studies have shown that energy shifts of valence and conduction states are nearly equal in topological insulators[49,50]. In case of YbMg₂Bi₂, the observed band structure shift is nearly-rigid, similar to that observed in other topological insulators[49,50].

Comparison between experimental and theoretical band dispersions: CaMg₂Bi₂

Figure 6 shows a comparison between the experimental and the calculated electronic structure of CaMg₂Bi₂. Figure 6a represents the ARPES spectrum close to the K̄ − Γ̄ − K̄ line. Theoretical electronic structures along the Γ-K and A-H lines are superimposed on Fig. 6a. It is clear that most of the spectral features are well reproduced by the calculation, except for the states indicated by an arrow. For better visualization of the states in the vicinity of E_F, a high-resolution ARPES spectrum is shown in Fig. 6b and its second derivative in Fig. 6c. It is evident that two sets of hole-like bands cross the Fermi level. The FS and a constant energy contour (at −0.1 eV) formed by these bands are shown in Fig. 6d, e, respectively. The shape of these contours is similar to that for YbMg₂Bi₂ and well reproduced by the theoretical calculation, as shown in Fig. 6f.

Figure 6g–i show the calculated surface electronic spectra from a (001) semi-infinite slab terminated by Ca, Mg, and Bi, respectively. As in the case of YbMg₂Bi₂, a TSS (indicated by arrows) is present on every termination. In addition to the TSS, the Bi-terminated surface shows trivial surface states near the VBM that are absent on the Ca- and Mg-terminated surfaces. These surface states originate from the unsaturated surface dangling bonds[51,52]. The absence of such states in the measured spectra (Fig. 6a–c) indicates that the surface is not Bi-terminated. Direct comparisons with the calculated spectra for Ca and Mg terminations are shown in Figs. 6j, k, respectively. Spectral features around Γ̄ are in somewhat better agreement with the Ca-termination,
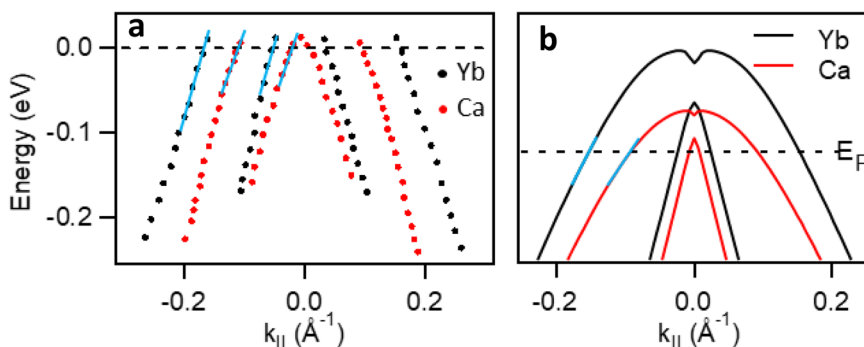
Fig. 7 Comparison of valence bands in YbMg$_2$Bi$_2$ and CaMg$_2$Bi$_2$. a MDC-derived bands of YbMg$_2$Bi$_2$ and CaMg$_2$Bi$_2$ near the Fermi level. The black (red) circles correspond to YbMg$_2$Bi$_2$ (CaMg$_2$Bi$_2$). Band slopes at E_F are highlighted by light-blue lines. **b** Shapes of the valence bands from our calculations. The CaMg$_2$Bi$_2$ spectra is shifted downward by 0.15 eV to reproduce the experimental features. Experimental E_F position is marked by dotted-line.

while near $\overline{K}$ the agreement is better with the Mg termination. Therefore, the coexistence of Mg and Ca terminations would probably give the best agreement with the observed spectra. The AFM measurements (Supplementary note 7) showing different step heights support that scenario.

We note that according to the Zintl formalism both YbMg$_2$Bi$_2$ and CaMg$_2$Bi$_2$ should be nominally charge balanced and predicted to be narrow-gap semiconductors. However, samples are usually highly *p*-doped, suggesting that holes are generated due to intrinsic defects[30]. According to the previous Hall studies[21,30], the estimated values of carrier concentrations and mobilities are lower in CaMg$_2$Bi$_2$ than in the rare-earth-based compounds YbMg$_2$Bi$_2$ and EuMg$_2$Bi$_2$. From ARPES measurements it is also possible to estimate the carrier concentrations by measuring the volume of the FS. In Fig. 7a, the MDC-derived bands crossing the Fermi level in YbMg$_2$Bi$_2$ and CaMg$_2$Bi$_2$ are plotted together. The Fermi wave vectors (k_F) of both inner and outer bands are larger in YbMg$_2$Bi$_2$ than in CaMg$_2$Bi$_2$, implying higher carrier concentrations. By assuming an isotropic spherical shape of the two FSs, formed by the two hole-like bands, we estimate the hole concentrations to be $\sim 1.4 \times 10^{20}$ cm^{-3} and $\sim 5 \times 10^{19}$ cm^{-3} for YbMg$_2$Bi$_2$ and CaMg$_2$Bi$_2$, respectively. The values estimated from the Hall coefficient are 4.6×10^{19} cm^{-3} and 1.7×10^{19} cm^{-3}, respectively[30]. Also, CaMg$_2$Bi$_2$ has a lower Fermi velocity than YbMg$_2$Bi$_2$. This behavior can be realized by putting the calculated valence bands of both materials on the same graph with their observed fillings (Fig. 7b).

Based on the shape and sharpness of the ARPES spectra, it seems that the effective masses and scattering rates are similar in these systems, which could lead to similar mobilities. However, the exact quantification of mobility is not possible from ARPES as the transport scattering rates are, in general, different from quasiparticle ones and the relationship between the effective mass and mobility for non-parabolic bands might be quite complex[53]. Moreover, the origin of higher mobilities in YbMg$_2$Bi$_2$ is still unclear and remains an open question.

We note that in predicting/interpreting the thermoelectric properties of these classes of materials, some studies disregarded SOC[25,38–40], leading to overestimated gaps, while the experiments and inclusion of SOC in calculations led to better agreement.

In summary, we have probed the electronic structure of the Zintl-phase isostructural analogs YbMg$_2$Bi$_2$ and CaMg$_2$Bi$_2$ using ARPES studies complemented with first-principles calculations. It is shown that the different carrier concentrations in these materials appear primarily due to a relative shift in E_F with respect to the valence band edge. Our results confirmed that the localized 4*f* electrons do not play a considerable role in the low-energy electronic structure of YbMg$_2$Bi$_2$. We have also

shown the importance of the SOC effect in these materials. Calculations suggest that these materials are narrow-band-gap topological insulators that support topological surface states with helical spin-texture. Due to the intrinsic hole doping, the actual E_F is located well inside the valence bands in these materials, which further restricts the effect of nontrivial band topology to be reflected in the transport properties. By tuning the E_F to the bulk band gap through chemical substitution or strain could lead to the observation of anomalous surface transport properties such as Shubnikov-de Haas oscillations, opening the possibility for their use in spintronics applications.

METHODS

Single crystal growth

Single crystals of CaMg$_2$Bi$_2$ and YbMg$_2$Bi$_2$ were grown with the self-flux solution-growth technique. The high-purity starting materials Ca (99.999%), Mg (99.98%), Bi (99.9999%) from Alfa Aesar and Yb from Ames Laboratory were used in nominal compositions CaMg$_4$Bi$_6$ and YbMg$_4$Bi$_6$. The elements were placed into alumina crucibles and sealed under $\approx$ 1/4 atm of high-purity inert Ar gas inside silica tubes. The assembly was then heated to 900 °C at a rate of 50 °C/h where the temperature was maintained for 12 h. The tubes were then cooled to 850 °C in 1 h followed by cooling to 750 °C in 10 h and finally to 650 °C in 24 h. Bulk three-dimensional-shaped single crystals with trigonal facets were obtained by removing the excess flux using a centrifuge at the last temperature.

Experimental details

Bulk structural characterizations were carried out by room-temperature powder x-ray diffraction (XRD) measurements on crushed single crystals using a Rigaku Geigerflex x-ray diffractometer with Cu-K$_\alpha$ radiation. The structural refinement was performed through Rietveld refinement using FULLPROF software package[42]. For the ARPES measurements, the samples were mounted on a sample holder and cleaved in-situ just before the measurements. The surface structure of the cleaved surface was checked using low-energy electron diffraction (LEED) and an atomic-force microscope (AFM) (Digital Instruments, NanoScope III). The ARPES experiments were carried out at OASIS-laboratory at Brookhaven National Laboratory using a Scienta SES-R4000 electron spectrometer with monochromatized He I$_\alpha$ (21.22 eV) and He II$_\alpha$ (40.8 eV) radiation (VUV-5k)[54]. The total instrumental energy resolution was $\sim$ 10 meV for He I$_\alpha$ and 20 meV for He II$_\alpha$. The angular resolution was better than 0.15° and 0.4° along and perpendicular to the slit of the analyzer, respectively. Most of the data were taken at $\sim$ 20 K.

Theoretical details

First-principles calculations have been carried out using Quantum ESPRESSO[55–57]. For the exchange and correlation energy/potential we used the PBEsol functional[58]. The projected-augmented-wave[59] method has been used to represent the core electrons. All the calculations have

been carried out using experimental lattice parameter, as noted in the 'structural details of samples' subsection. The cut-off energy for the plane waves and charge density were set to 60 Ry and 520 Ry, respectively. A k-mesh of $12 \times 12 \times 10$ has been used for the Brillouin-zone integration. The electronic structure calculations have been carried out both with and without SOC. Pw2wannier interface and WANNIER90 were used for the construction of the first-principle tight binding Hamiltonian[60]. Surface-states spectra have been calculated using the WANNIERTOOLS package[61].

DATA AVAILABILITY

The data that support the findings of this study are available from the corresponding author upon reasonable request.

REFERENCES

1. Dusastre, V. Materials for Sustainable Energy (World Scientific, 2010).
2. DiSalvo, F. J. Thermoelectric cooling and power generation. *Science* **285**, 703–706 (1999).
3. He, J. & Tritt, T. M. Advances in thermoelectric materials research: Looking back and moving forward. *Science* **357**, eaak9997 (2017).
4. Gascoin, F., Ottensmann, S., Stark, D., Haïle, S. M. & Snyder, G. J. Zintl phases as thermoelectric materials: tuned transport properties of the compounds $Ca_xYb_{1-x}Zn_2Sb_2$. *Adv. Funct. Mater.* **15**, 1860–1864 (2005).
5. Pakhira, S. et al. Zero-field magnetic ground state of $EuMg_2Bi_2$. *Phys. Rev. B* **103**, 024408 (2021).
6. Xu, Y., Song, Z., Wang, Z., Weng, H. & Dai, X. Higher-order topology of the axion insulator $EuIn_2As_2$. *Phys. Rev. Lett.* **122**, 256402 (2019).
7. Regmi, S. et al. Temperature-dependent electronic structure in a higher-order topological insulator candidate $EuIn_2As_2$. *Phys. Rev. B* **102**, 165153 (2020).
8. Li, H. et al. Dirac surface states in intrinsic magnetic topological insulators $EuSn_2As_2$ and $MnBi_{2n}Te_{3n+1}$. *Phys. Rev. X* **9**, 041039 (2019).
9. Pakhira, S., Tanatar, M. A., Heitmann, T., Vaknin, D. & Johnston, D. C. A-type antiferromagnetic order and magnetic phase diagram of the trigonal Eu spin- 7/2 triangular-latticecompound $EuSn_2As_2$. *Phys. Rev. B* **104**, 174427 (2021).
10. Takane, D. et al. Dirac semimetal phase and switching of band inversion in XMg_2Bi_2 ($X =$ Ba and Sr). *Sci. Rep.* **11**, 21937 (2021).
11. Chang, T.-R. et al. Realization of a type-II nodal-line semimetal in Mg_3Bi_2. *Adv. Sci.* **6**, 1800897 (2019).
12. Marshall, M. et al. Magnetic and electronic structures of antiferromagnetic topological material candidate $EuMg_2Bi_2$. *J. Appl. Phys.* **129**, 035106 (2021).
13. Kabir, F. et al. Observation of multiple Dirac states in a magnetic topological material $EuMg_2Bi_2$. Preprint at https://arxiv.org/abs/1912.08645 (2019).
14. Pakhira, S. et al. A-type antiferromagnetic order in semiconducting $EuMg_2Sb_2$ single crystals. Preprint at https://arxiv.org/abs/2204.05261 (2022).
15. Petrov, E. K., Silkin, I. V., Koroteev, Y. M. & Chulkov, E. V. Effect of deformation on the electronic structure and topological properties of the $A^{II}Mg_2Bi_2$ ($A^{II} =$ Mg, Ca, Sr, Ba) compounds. *JETP Lett.* **105**, 502–507 (2017).
16. Valla, T., Pan, Z.-H., Gardner, D., Lee, Y. S. & Chu, S. Photoemission spectroscopy of magnetic and nonmagnetic impurities on the surface of the Bi_2Se_3 topological insulator. *Phys. Rev. Lett.* **108**, 117601 (2012).
17. Li, Q. et al. Chiral magnetic effect in Zr_2Te_5. *Nat. Phys.* **12**, 550–554 (2016).
18. Hoefer, K., Becker, C., Wirth, S. & Hao Tjeng, L. Protective capping of topological surface states of intrinsically insulating Bi_2Te_3. *AIP Adv.* **5**, 097139 (2015).
19. Chen, X. et al. Extraordinary thermoelectric performance in n-type manganese doped Mg_3Sb_2 Zintl: high band degeneracy, tuned carrier scattering mechanism and hierarchical microstructure. *Nano Energy* **52**, 246–255 (2018).
20. Sun, J. & Singh, D. J. Thermoelectric properties of AMg_2X_2, AZn_2Sb_2 (A = Ca, Sr, Ba; X = Sb, Bi), and Ba_2ZnX_2 (X = Sb, Bi) Zintl compounds. *J. Mater. Chem. A* **5**, 8499–8509 (2017).
21. Shuai, J. et al. Higher thermoelectric performance of Zintl phases $(Eu_{0.5}Yb_{0.5})_{1-x} Ca_xMg_2Bi_2$ by band engineering and strain fluctuation. *Proc. Nat. Acad. Sci.* **113**, E4125–E4132 (2016).
22. Wang, X. et al. Experimental revelation of multiband transport in heavily doped $BaCd_2Sb_2$ with promising thermoelectric performance. *Mater. Today Phys.* **8**, 123–127 (2019).
23. Wang, J. et al. Enhanced thermoelectric properties of Zintl phase $YbMg_2Bi_{1.98}$ through Bi site substitution with Sb. *J. Mater. Sci. Technol.* **59**, 189–194 (2020).
24. Guo, M. et al. Enhanced thermoelectric performance of p-type $CaMg_2Bi_{1.98}$ and optimized $CaAl_2Si_2$-type Zintl phase module with equal cross-section area. *Mater. Today Phys.* **15**, 100270 (2020).
25. Zhang, J. et al. Designing high-performance layered thermoelectric materials through orbital engineering. *Nat. Commun.* **7**, 10892 (2016).
26. Toberer, E. S., May, A. F., Melot, B. C., Flage-Larsen, E. & Snyder, G. J. Electronic structure and transport in thermoelectric compounds AZn_2Sb_2 (A = Sr, Ca, Yb, Eu). *Dalton Trans.* **39**, 1046–1054 (2010).
27. Sun, J., Shuai, J., Ren, Z. & Singh, D. J. Computational modelling of the thermoelectric properties of p-type Zintl compound $CaMg_2Bi_2$. *Mater. Today Phys.* **2**, 40–45 (2017).
28. Pakhira, S., Tanatar, M. A. & Johnston, D. C. Magnetic, thermal, and electronic-transport properties of $EuMg_2Bi_2$ single crystals. *Phys. Rev. B* **101**, 214407 (2020).
29. May, A. F. et al. Thermoelectric transport properties of $CaMg_2Bi_2$, $EuMg_2Bi_2$, and $YbMg_2Bi_2$. *Phys. Rev. B* **85**, 035202 (2012).
30. May, A. F., McGuire, M. A., Singh, D. J., Custelcean, R. & Jellison, G. E. Jr Structure and properties of single crystalline $CaMg_2Bi_2$, $EuMg_2Bi_2$, and $YbMg_2Bi_2$. *Inorg. chem.* **50**, 11127–11133 (2011).
31. Wang, S., Li, H., Lu, R., Zheng, G. & Tang, X. Metal nanoparticle decorated n-type Bi_2Te_3-based materials with enhanced thermoelectric performances. *Nanotechnology* **24**, 285702 (2013).
32. Flage-Larsen, E., Diplas, S., Prytz, Ø., Toberer, E. S. & May, A. F. Valence band study of thermoelectric Zintl-phase $SrZn_2Sb_2$ and $YbZn_2Sb_2$: X-ray photoelectron spectroscopy and density functional theory. *Phys. Rev. B* **81**, 205204 (2010).
33. Pei, Y. et al. Convergence of electronic bands for high performance bulk thermoelectrics. *Nature* **473**, 66–69 (2011).
34. Pei, Y., Wang, H., Gibbs, Z. M., LaLonde, A. D. & Snyder, G. J. Thermopower enhancement in $Pb_{1-x}Mn_xTe$ alloys and its effect on thermoelectric efficiency. *NPG Asia Mater.* **4**, e28–e28 (2012).
35. Liu, W. et al. Convergence of conduction bands as a means of enhancing thermoelectric performance of n-type $Mg_2Si_{1-x}Sn_x$ solid solutions. *Phys. Rev. Lett.* **108**, 166601 (2012).
36. Fu, C. et al. High band degeneracy contributes to high thermoelectric performance in p-type half-Heusler compounds. *Adv. Energy Mater.* **4**, 1400600 (2014).
37. Xie, H. et al. Beneficial contribution of alloy disorder to electron and phonon transport in half-Heusler thermoelectric materials. *Adv. Funct. Mater.* **23**, 5123–5130 (2013).
38. Gong, J. et al. Investigation of the bipolar effect in the thermoelectric material $CaMg_2Bi_2$ using a first-principles study. *Phys. Chem. Chem. Phys.* **18**, 16566–16574 (2016).
39. Wang, X., Lu, Y., Hu, Z. & Shao, X. Theoretical study on thermoelectric properties and doping regulation of Mg_3X_2 ($X =$ As, Sb, Bi). *Metals* **11**, 6 (2021).
40. Zhou, T. et al. Thermoelectric properties of Zintl phase $YbMg_2Sb_2$. *Chem. Mater.* **32**, 776–784 (2020).
41. Momma, K. & Izumi, F. VESTA3 for three-dimensional visualization of crystal, volumetric and morphology data. *J. Appl. Crystallogr.* **44**, 1272–1276 (2011).
42. Rodrguez-Carvajal, J. Recent advances in magnetic structure determination by neutron powder diffraction. *Phys. B* **192**, 55–69 (1993).
43. Yu, R., Qi, X. L., Bernevig, A., Fang, Z. & Dai, X. Equivalent expression of Z_2 topological invariant for band insulators using the non-Abelian Berry connection. *Phys. Rev. B* **84**, 075119 (2011).
44. Antonov, V., Harmon, B. & Yaresko, A. Electronic structure of mixed-valence semiconductors in the LSDA + U approximation. II. SmB_6 and YbB_{12}. *Phys. Rev. B* **66**, 165209 (2002).
45. Zhou, T. et al. Experimental evidence of topological surface states in Mg_3Bi_2 films grown by molecular beam epitaxy. *Chin. Phys. Lett.* **36**, 117303 (2019).
46. Fujii, J. et al. Mitrofanovite Pt_3Te_4: A topological metal with termination-dependent surface band structure and strong spin polarization. *ACS Nano* **15**, 14786–14793 (2021).
47. Iwasawa, H. et al. Buried double CuO chains in $YBa_2Cu_4O_8$ uncovered by nano-ARPES. *Phys. Rev. B* **99**, 140510 (2019).
48. Gibson, Q. D. et al. Termination-dependent topological surface states of the natural superlattice phase Bi_4Se_3. *Phys. Rev. B* **88**, 081108 (2013).
49. Bianchi, M. et al. Coexistence of the topological state and a two-dimensional electron gas on the surface of Bi_2Se_3. *Nat. Commun.* **1**, 128 (2010).
50. Kim, C. K., Denlinger, J. D., Kundu, A. K., Gu, G. & Valla, T. Absence of a Dirac gap in ferromagnetic $Cr_x(Bi_{0.1}Sb_{0.9})_{2-x} Te_3$. *J. Appl. Phys.* **129**, 083902 (2021).
51. Zhu, X.-G. et al. Electronic structures of topological insulator Bi_2Te_3 surfaces with non-conventional terminations. *N. J. Phys.* **18**, 093015 (2016).
52. Tan, R. et al. Double band inversion in the topological phase transition of $Ge_{1-x}Sn_x$ alloys. *Europhys. Lett.* **133**, 57001 (2021).
53. Pan, Z.-H. et al. Measurement of an exceptionally weak electron-phonon coupling on the surface of the topological insulator Bi_2Se_3 using angle-resolved photoemission spectroscopy. *Phys. Rev. Lett.* **108**, 187001 (2012).

54. Kim, C. K. et al. In-situ angle-resolved photoemission spectroscopy of copper-oxide thin films synthesized by molecular beam epitaxy. *J. Electron Spectrosc. Relat. Phenom.* https://doi.org/10.1016/j.elspec.2018.07.003 (2018).

55. Giannozzi, P. et al. Quantum Espresso: a modular and open-source software project for quantum simulations of materials. *J. Phys. Condens. Matter* **21**, 395502 (2009).

56. Giannozzi, P. et al. Advanced capabilities for materials modelling with Quantum Espresso. *J. Phys. Condens. Matter* **29**, 465901 (2017).

57. Giannozzi, P. et al. Quantum Espresso toward the exascale. *J. Chem. Phys.* **152**, 154105 (2020).

58. Perdew, J. P. et al. Restoring the density-gradient expansion for exchange in solids and surfaces. *Phys. Rev. Lett.* **100**, 136406 (2008).

59. Blöchl, P. E. Projector augmented-wave method. *Phys. Rev. B* **50**, 17953–17979 (1994).

60. Mostofi, A. A. et al. An updated version of wannier90: a tool for obtaining maximally-localised wannier functions. *Comput. Phys. Commun.* **185**, 2309–2310 (2014).

61. Wu, Q., Zhang, S., Song, H.-F., Troyer, M. & Soluyanov, A. A. Wanniertools: an open-source software package for novel topological materials. *Comput. Phys. Commun.* **224**, 405–416 (2018).

AUTHOR CONTRIBUTIONS

A.K.K. designed the study, performed ARPES experiments and written the manuscript with a key contribution from T.R. and S.P. A.K.K., and T.V. analyzed the ARPES data. T.R. performed the theoretical electronic structure calculation. S.P. grew the bulk single-crystals and performed the physical characterization. Z.W. performed the AFM measurements. T.V. and D.C.J. edited the manuscript. All the authors discussed the results and reviewed the manuscript. T.V. made contributions to development of the OASIS facility used herein.

COMPETING INTERESTS

The authors declare no competing interests.

ADDITIONAL INFORMATION

Supplementary information The online version contains supplementary material available at https://doi.org/10.1038/s41535-022-00474-2.

Correspondence and requests for materials should be addressed to Asish K. Kundu.

Reprints and permission information is available at http://www.nature.com/reprints

Publisher's note Springer Nature remains neutral with regard to jurisdictional claims in published maps and institutional affiliations.